Quantum Chemical Simulation of Carbon Nanotube Nucleation on Al₂O₃ Catalysts via CH₄ Chemical Vapor Deposition

Alister J. Page,*,⊥,† Supriya Saha,⊥,† Hai-Bei Li,§ Stephan Irle,*,‖ and Keiji Morokuma*,‡

†Newcastle Institute for Energy and Resources, The University of Newcastle, Callaghan 2308, Australia
‡Fukui Institute for Fundamental Chemistry, Kyoto University, Kyoto 606-8103, Japan
§School of Ocean, Shandong University, Weihai 264209, China
‖Institute of Transformative Bio-Molecules (WPI-ITbM) and Department of Chemistry, Graduate School of Science, Nagoya University, Nagoya 464-8602, Japan

S Supporting Information

ABSTRACT: We present quantum chemical simulations demonstrating how single-walled carbon nanotubes (SWCNTs) form, or "nucleate", on the surface of Al_2O_3 nanoparticles during chemical vapor deposition (CVD) using CH_4. SWCNT nucleation proceeds via the formation of extended polyyne chains that only interact with the catalyst surface at one or both ends. Consequently, SWCNT nucleation is not a surface-mediated process. We demonstrate that this unusual nucleation sequence is due to two factors. First, the π interaction between graphitic carbon and Al_2O_3 is extremely weak, such that graphitic carbon is expected to desorb at typical CVD temperatures. Second, hydrogen present at the catalyst surface actively passivates dangling carbon bonds, preventing a surface-mediated nucleation mechanism. The simulations reveal hydrogen's reactive chemical pathways during SWCNT nucleation and that the manner in which SWCNTs form on Al_2O_3 is fundamentally different from that observed using "traditional" transition metal catalysts.
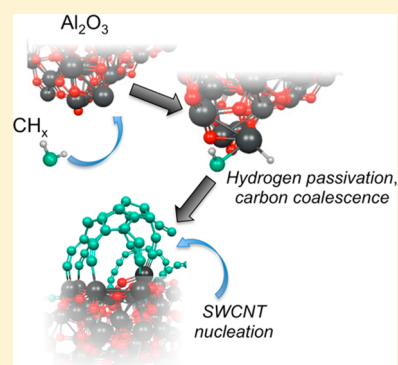
1. INTRODUCTION

The discovery of single-walled carbon nanotubes (SWCNTs) in the early 1990s[1−3] was a landmark moment in nanoscience and nanotechnology. Since their discovery, the outstanding mechanical, optical, and electronic properties of SWCNTs have driven intense research efforts into the optimization of their synthesis. The optical and electronic properties of a SWCNT are determined by its chiral indices, (n,m). Electronic and optical devices based on SWCNTs are therefore limited by our ability to synthesize and isolate single types of (n,m) SWCNTs. The development of such synthetic methods (so-called "chirality-controlled" growth) has therefore been the ultimate goal of SWCNT growth science for the past two decades.

SWCNTs were originally produced via carbon arc discharge with transition metal catalysts.[1−3] Today, however, by far the most common family of techniques for SWCNT production is chemical vapor deposition (CVD) on catalytic nanoparticles. Recently a number of important achievements have been made toward the goal of chirality-controlled SWCNT growth by a number of groups.[4] These approaches have combined CVD techniques with "amplification" growth,[5,6] cloning,[7,8] catalyst design,[9−12] and templated organic synthesis.[13−21]

Of these approaches, catalyst design is arguably the most versatile and accessible method. Recent studies[12] have demonstrated that keeping the catalyst nanoparticle solid during growth is a key factor enabling the production of extremely narrow (n,m) distributions. In this respect, the use of

"nontraditional" CVD catalysts, such as semiconducting Si and Ge,[22] SiC,[22−24] SiO₂,[25−29] ZrO₂,[30] Al₂O₃,[31] and even diamond[32] and fullerenes[33] are potentially ideal candidate nanoparticles for initiating chirality-controlled growth, since all of them (except Ge[22]) remain in the solid state at typical CVD temperatures. However, the lower catalytic activities of these nonmetallic nanoparticles in the solid state result in relatively low SWCNT yields. SWCNT nucleation and growth mechanisms on Si, SiC, and SiO₂ have been studied extensively.[34−37] While SWCNT growth has been demonstrated using these other nonmetallic nanoparticles, the atomistic mechanism underpinning nucleation and growth in each case remains unexplained. However, understanding the nucleation and growth processes at the atomic level is the key to achieving chirality control using these nontraditional catalysts.

Herein we present the first investigation establishing how CH₄ CVD proceeds on Al₂O₃ nanoparticles, leading to SWCNT nucleation. Quantum chemical molecular dynamics (QM/MD) simulations are used to model the CVD process at 1100 K and show that SWCNT nucleation on Al₂O₃ proceeds via polyyne chain cross-linking *away* from the Al₂O₃ nanoparticle surface,[38] between chains that are only anchored at one or both ends. This process resembles fullerene formation[39]

more closely than it does SWCNT nucleation on transition metal and Si-based catalysts and so is a marked departure from established nucleation mechanisms. Density functional theory calculations reveal that this mechanism arises from a combination of (1) the extremely weak carbon−Al_2O_3 π-interaction and (2) hydrogen's capacity to preferentially passivate particular surface-adsorbed carbon species. The simulations presented here will hopefully assist in understanding how solid phase "catalysts" such as Al_2O_3 can be exploited toward chirality-controlled SWCNT growth.

2. COMPUTATIONAL DETAILS

2.1. Quantum Chemical Methods. Nonequilibrium QM/MD simulations were based on the self-consistent charge density functional tight binding method (SCC-DFTB)[40] as implemented in the DFTB+ program,[41] with the matsci-0-2 parameters.[42] The quantum chemical potential energy and energy derivatives were calculated on the fly at each step in the MD simulation. Equations of motion were integrated according to the velocity-Verlet[43] algorithm using a time step of 0.5 ps. The temperature was maintained throughout all simulations at 1100 K via a Nosé−Hoover chain thermostat (chain length 3)[44,45] coupled to the degrees of freedom of the system. An electronic temperature[46−48] of 1500 K was also enforced during each SCC cycle. The occupancies of molecular orbitals close to the Fermi level were therefore not necessarily integer-occupied; instead they were described using a Fermi−Dirac distribution function of the orbital energy. Such an electron smearing approach has been used extensively by our group in the context of nanoscale self-assembly[29,34−36,49−53] and is also standard practice in traditional first-principles-based MD simulations. A practical advantage of electron smearing is that the rate of convergence of the SCC cycles at each step of the MD simulation is substantially accelerated. Furthermore, the use of a finite electronic temperature is essential in systems such as those employed here, due to the presence of numerous carbon and aluminum dangling bonds.

Density functional theory (DFT) was employed to calculate adsorption energies of CH_x ($x = 0−3$) and hydrogen atoms on Al_2O_3, reaction energies for CH_4 dehydrogenation, and graphene adsorption energies. The PBE exchange-correlation functional[54] was utilized in conjunction with a valence double-ζ plus polarization function (DZP) basis set, and norm-conservative Troullier−Martins pseudopotentials for core electrons. An electronic temperature of 1500 K was applied to all DFT calculations, for consistency with DFTB results. A ($1 \times 1 \times 1$) k-point sampling scheme and a Mesh-cutoff of 150 Ry were employed to ensure adequate convergence. All DFT calculations employed the SIESTA program.[55]

2.2. Model Systems and SWCNT Growth Simulations. SWCNT nucleation on Al_2O_3 nanoparticle catalysts has been simulated here in a similar manner to that used previously for Si-based catalysts[34,35] and transition metal catalysts.[49,50,56] The model catalyst was an Al-terminated $Al_{60}O_{83}$ nanoparticle, cleaved from the bulk Al_2O_3 corundum structure[57] (see Figure S1). The approximate dimensions of this nanoparticle were $2 \times 2 \times 2$ nm³. For all simulations, this nanoparticle was placed at the center of a $6 \times 6 \times 6$ nm³ cubic supercell, before being optimized at 0 K. This optimized structure was then equilibrated using MD at 1100 K; 10 trajectories were generated using randomly chosen initial velocities (according to a Boltzmann distribution) for all atoms in the catalyst. All subsequent CVD simulations were also replicated 10 times.

The CVD process was simulated here via the periodic addition of carbonaceous radical feedstock. To ascertain the role of hydrogen in this process, we have investigated the Al_2O_3-catalyzed CVD processes via two sets of simulations that model the presence and absence of hydrogen. For the latter scenario, carbon atoms were adsorbed onto the Al_2O_3 nanoparticle surface at intervals of 1 ps. For the former scenario, CH_x ($x = 0, ..., 3$) were adsorbed onto the surface of the Al_2O_3 nanoparticle at intervals of 1 ps. This approach, as opposed simply to the addition of CH_4 (which resulted only in nonreactive collisions), is justified by previous experimental suggestions[27] that CH_4

molecules partially decompose pyrolytically under typical CVD conditions, prior to adsorbing on the catalyst surface. The value of x here was chosen randomly but weighted via a Poisson distribution so as to reflect the thermodynamics of successive dehydrogenation of CH_4 (i.e., CH_3 was more probable than CH_2, and so on). It can safely be assumed that such CH_x dissociation products are present in low concentrations under CVD conditions and that follow-up reactions of radicals on the nanoparticle surface actively contribute to their generation via hydrogen abstraction reactions. Each adsorption site for both CH_x radicals and C atoms was chosen randomly, and the initial velocities of all adsorbed atoms satisfied a Boltzmann distribution at 1100 K. The velocities of the feedstock particles were directed toward the center of mass of the Al_2O_3 nanoparticle. Following 20 ps, hydrogens were randomly removed from the simulation at a rate of 2 H/ps. This approach effectively mimics the natural chemical removal of hydrogen atoms prevalent in high temperature conditions, such as those observed in CVD chambers, for instance by water formation. We have used this approach in previous investigations of SWCNT nucleation,[35] giant fullerene formation,[58] and polyaromatic hydrocarbon formation.[59] For the latter scenario, i.e. CVD in the absence of hydrogen, atomic carbon was adsorbed onto the model Al_2O_3 catalyst surface at a rate of 2 C/ps.

DFT calculations employ a $[2 \times 2 \times 1]$ extension of the Al-terminated $Al_2O_3[0001]$ unit cell (see Figure S2). Three-dimensional periodic boundary conditions were employed, with a vacuum region of 5 nm between adjacent surfaces to prevent undesired surface−surface interactions. The lattice parameters ($a = 0.4757$ nm and $b = 1.2987$ nm) were fixed at the experimental values.[57] The Al-terminated Al_2O_3 surface employed here has only two symmetrically distinct Al atoms present at the surface (denoted A and B in Figure S2). Here we only consider H/CH_x adsorption on Al atom A; adsorption at the Al atom B is not considered here due to steric and coordination considerations (although it has been previously shown for H that adsorption at atom B is possible[60]).

3. RESULTS AND DISCUSSION

3.1. SWCNT Nucleation Mechanism on Al_2O_3 Nanoparticles. An example of SWCNT nucleation observed in the absence of hydrogen (trajectory 3) is depicted in Figure 1. Figure S3 shows snapshots from each individual QM/MD trajectory at comparable times (beyond 100 ps), when the adsorbed carbon densitiy on the Al_2O_3 surface is the same for all trajectories.[61] Two observations can be made immediately from these figures. First, much of the carbon applied to the Al_2O_3 nanoparticle surface desorbs, in the form of isolated C
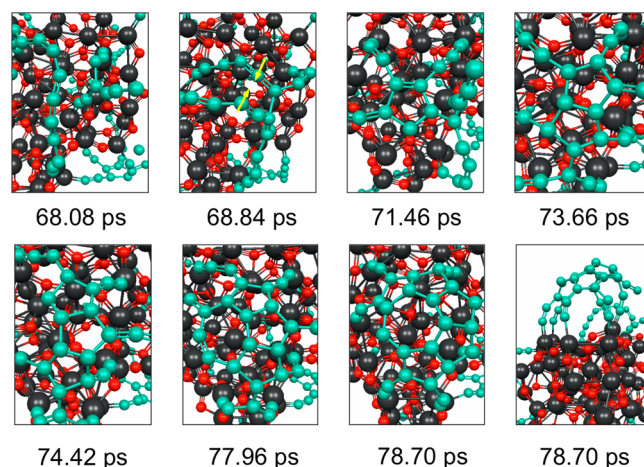

68.08 ps   68.84 ps   71.46 ps   73.66 ps

74.42 ps   77.96 ps   78.70 ps   78.70 ps

Figure 1. Example of Al_2O_3-catalyzed SWCNT nucleation mechanism observed in QM/MD simulations. Black spheres: Al atoms. Red spheres: O atoms. Cyan spheres: C atoms.

atoms, small fragments, or extended C_n polyyne chains. This follows from the relatively weak Al−C bond,[62] which, as we will discuss below, is a key factor that determines the nature of SWCNT nucleation on Al_2O_3 catalysts. Second, the carbon that remains adsorbed exists predominantly as long polyyne chains anchored to the surface at either one or both ends by σ-type C−Al bonds. These chains undergo free translational and vibrational diffusion in the surrounding atmosphere due to their minimal interaction with the catalyst surface along the length of the chain (discussed further below).

Consequently, SWCNT nucleation occurs via a mechanism more akin to fullerene formation[39] than to SWCNT nucleation on iron-group transition metals[49,51,63,64] and Si-based catalysts.[34−37] The latter are both surface-mediated processes due to the strengths of the catalyst−carbon σ/π interactions. We return to a full discussion of this comparison below. Here we focus on the mechanism of Al_2O_3-catalyzed SWCNT growth, since to our knowledge no such mechanism has been reported previously.

Due to the weakness of the Al_2O_3-carbon π-interaction, the SWCNT nucleation mechanism observed here closely resembles Eres' polyyne oligomerization mechanism.[38] These simulations also suggest that, as for SWCNT nucleation with Si-based catalysts, surface saturation with carbon is a prerequisite for SWCNT nucleation. For example, the formation of the SWCNT cap in Figure 1 begins with the coalescence of two adjacent polyyne chains, indicated by yellow arrows (68.84 ps). Both of these chains are substantial in length, consisting of 16 and 9 carbon atoms, respectively. It is also noted here that both carbon chains contain polyyne Y-junctions; the formation of these junctions has been shown to be a crucial step in SWCNT/graphene nucleation on iron-group transition metal catalysts, producing typically a pentagon as the first carbon ring species. However, this is presumably not the case here, since the coalescence of these two chains occurs independently of these junctions. Between ca. 68 and 71 ps these two carbon chains form C−C bonds on a number of occasions. However, due to their high translational and vibrational mobility, these C−C bonds typically break soon afterward. This is even the case for thermodynamically stable pentagons, which were formed and broken several times (between ca. 71 and 73 ps). This is unusual for SWCNT nucleation; however, this has been reported during fullerene formation.[39] Polygonal carbon rings are only stabilized when a number of them coalesce almost simultaneously (between 73 and 74 ps). For example, in this trajectory, three pentagons form next to each other within approximately 3 ps, after which a single heptagon is formed. Within a further 1 ps another two pentagons form to give the final cap structure (78.70 ps) shown in Figure 1.

Ultimately this SWCNT cap consists of five pentagons and a single heptagon. The predominance of pentagons over hexagons in this example (and all others observed during these simulations) is peculiar among all other examples of SWCNT nucleation using, for example, iron-group transition metals[51,63,64] and Si-group catalysts.[34−37] However, it follows from the fact that both of the polyyne chains shown in Figure 1 are anchored to the Al_2O_3 nanoparticle through terminating C−Al σ-bonds and "loop" away from the nanoparticle surface. Any polygonal carbon rings that subsequently form between them are forced to adopt a highly positive curvature; only pentagons can achieve this. Pentagon addition to the point of cap closure is prevented here by termination of carbon dangling

bonds by the Al_2O_3 surface (as predicted via Smalley's "Scooter mechanism"[65]), and this is consistent with the strength of these C−Al σ-bonds. Although they are not as strong as some transition metal C−M bonds,[62] they are strong enough to withstand the thermal energy observed at 1100 K. In this respect it is anticipated, on the basis of previous predictions,[66] that SWCNT diameter should be smaller than catalyst diameter for Al_2O_3, which is indeed observed in our QM/MD simulations.

Our discussion of the SWCNT nucleation mechanism here (Figures 1, S3) is based on carbon-only simulations. Although simulations with CH_x (as opposed to C atoms) were performed, no instance of SWCNT nucleation was observed over time scales of 100−200 ps. This is consistent with the previous work of Wang et al.,[67] who considered the role of H during Fe-catalyzed C_2H_2 CVD SWCNT nucleation. High hydrogen concentrations effectively terminated dangling σ carbon bonds. In turn this prevented the formation of a positively curved sp^2-carbon network and thus impeded SWCNT nucleation. Li et al.[59] have shown similar phenomena during the nucleation of polycyclic aromatic hydrocarbons during oxygen-lean benzene combustion. In the following section, we turn to a more detailed discussion on the role of hydrogen in the present simulations.

3.2. CH_4 CVD on Al_2O_3 Nanoparticles: The Role of Hydrogen. Liu et al.[31] have previously reported SWCNT growth using solid Al_2O_3 catalysts with ethanol feedstock in the presence of Ar/H_2. It was proposed that the H_2 present during Al_2O_3-catalyzed CVD promoted growth by displacing (or preventing the accumulation of) amorphous carbon from the catalyst surface, thereby preventing catalyst poisoning and making the catalyst active for a longer period of time. Here we consider both the thermochemical and dynamic aspects of surface carbon displacement by hydrogen.

The displacement of amorphous carbon from the Al_2O_3 surface would require a significant portion of the catalyst surface to be hydrogen passivated. Figure 2 shows that the transfer of hydrogen from surface-adsorbed carbon species onto the Al_2O_3 surface is observed during QM/MD simulations. This indicates that hydrogen passivation of surface Al atoms is plausible, even in the absence of ambient H_2. Similar observations were also reported recently for nickel catalysts.[68,69] Supplementary PBE calculations ensure that this is not an artifact of the DFTB parameters used in our MD simulations. For example, Figure 2a structures at 0 and 1.20 ps were optimized at 0 K using both SCC-DFTB and PBE/DZP (Figure S4). The energy associated with this hydrogen transfer reaction is 56.38 (SCC-DFTB) and 51.36 kcal/mol (PBE/DZP), which are in close agreement. Comparable agreement in the optimized reactant (0 ps) and product (1.20 ps) structures was also observed, as shown in Figure S4. Hydrogen abstraction observed during QM/MD simulations is consistent with the relative adsorption energies of H and CH_3 on Al_2O_3, given in Table 1. Adsorption energy is calculated here via

$$E_{ads} = E(X + Al_2O_3) - [E(X) + E(Al_2O_3)] \qquad (1)$$

where X = C, CH, CH_2, CH_3, and H. Table 1 shows that the Al−H bond is stronger than the Al−C (CH_3) bond by ∼4 kcal/mol using PBE/DZP. SCC-DFTB (not shown) predicts the same trend, although the difference in these calculated bond strengths is larger.

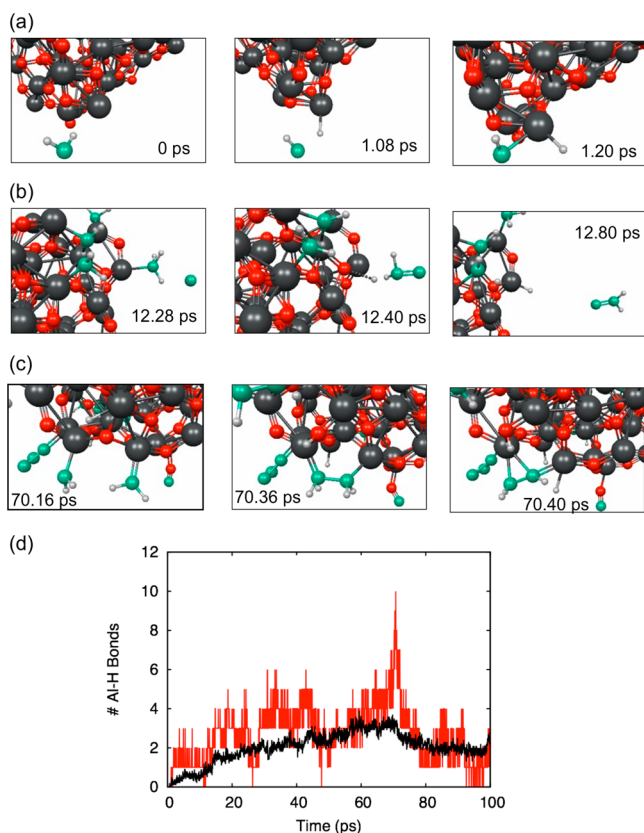If hydrogen were capable of displacing amorphous carbon from the Al_2O_3 surface, it would also have to be a

(a)

(b)

(c)

(d)

Figure 2. (a−c) Separate examples of Al$_2$O$_3$-catalyzed H and abstraction observed in QM/MD trajectory 4. H-abstraction is driven exclusively by surface Al atoms. (d) Population of Al−H bonds observed during trajectory 4 (red line) and averaged over all trajectories (black line).

Table 1. Adsorption energies E_{ads} (kcal/mol) for CH$_x$ and H on Al$_2$O$_3$ [0001]

C	CH	CH$_2$	CH$_3$	H
−108.2	−66.5	−122.2^a	−46.3	−50.7

^{a}PBE/DZP predicts CH$_2$ adsorbs via bond formation with both Al and O, causing an anomalous increase in E_{ads}.

thermochemically favorable process. In other words, E_{ads} for hydrogen would have to be substantially larger than E_{ads} for sp-, sp^2-, and sp^3-hybridized carbon (modeled here with C, CH, CH$_2$, and CH$_3$, respectively). E_{ads} values of H and CH$_3$ on Al$_2$O$_3$ are comparable, so the displacement of sp^3-hybridized carbon from Al$_2$O$_3$ by hydrogen passivation, while feasible, is unlikely to be a frequent process (consistent with our QM/MD simulations). For surface-adsorbed sp- and sp^2-hybridized carbon, E_{ads} for CH$_2$, CH, and C on Al$_2$O$_3$ are substantially larger than E_{ads} for hydrogen (E_{ads} for CH$_2$ is anomalously high since CH$_2$ adsorbs via C−Al and C−O bond formation). This effectively rules out displacement of these groups from the Al$_2$O$_3$ surface by hydrogen, at least on a thermochemical basis. Therefore, hydrogen is not necessarily capable of displacing all amorphous carbon species from the Al$_2$O$_3$ surface; it depends on the type of surface carbon that is present.

Instead, we propose an alternative mechanism by which hydrogen promotes SWCNT growth on Al$_2$O$_3$ catalysts. We propose that hydrogen promotes SWCNT growth not by displacement of surface-adsorbed carbon, but by promoting the formation of CH/CH$_2$ carbon species, which are capable of

polyyne chain formation. This is demonstrated by considering the dominant hydrogenation reactions occurring on the Al$_2$O$_3$ surface. Table 2 shows that hydrogenation of surface-adsorbed

Table 2. PBE/DZP Reaction Energies for Hydrogenation Reactions of Al$_2$O$_3$[0001] and Carbon Species Adsorbed on Al$_2$O$_3$[0001]

	ΔE (kcal/mol)
	−83.9
	−49.2
	−75.6
	−190.8
	−139.5
	−101.5
	−83.2
	−97.0
	−33.2

CH species, forming CH$_2$, is the most thermochemically favorable hydrogenation process during SWCNT nucleation on Al$_2$O$_3$, with ΔE = −190.8 kcal/mol. By comparison, ΔE values for hydrogenation of surface-adsorbed C and CH$_2$ are both ca. −83 kcal/mol. Combined with Table 1, this indicates that surface-adsorbed CH$_2$ are expected to be the most abundant species on the Al$_2$O$_3$ surface. Hydrogenation of Al$_2$O$_3$ aluminum and oxygen in the presence of adjacent CH$_2$ are the second and third most favorable reactions, with maximum ΔE values of −139.5 and −101.5 kcal/mol, respectively. We note that this is a substantial increase compared to the hydrogenation of pristine Al$_2$O$_3$[0001] (Table 1).

Surface-adsorbed H and CH$_2$ species will therefore be the dominant species during SWCNT nucleation on Al$_2$O$_3$. The formation and adsorption of CH groups on the Al$_2$O$_3$ surface are also thermochemically favorable. Since C−C bond formation is a highly exothermic process,[67] both CH and CH$_2$ groups will rapidly aggregate on the surface due to their carbon dangling bonds. Ultimately this will result in polyyne chain formation, consistent with our QM/MD simulations. The depletion in surface CH and CH$_2$ groups that results from this aggregation will drive further CH/CH$_2$ formation via Le Chatelier behavior. We note also that these chains extend away from the catalyst surface (due to the weaker carbon−catalyst π-interaction, discussed below), thereby keeping a larger portion

of the nanoparticle surface available for further carbon deposition.

With respect to CH_3, both formation and adsorption are less favorable than either CH or CH_2, as shown in Tables 1 and 2. Aggregation of CH_3 groups is also impossible, since there are no carbon dangling bonds available. Consequently, the saturation of the Al_2O_3 surface with "inactive" CH_3 species, which would otherwise obstruct SWCNT nucleation, is an unfavorable process.

This means that hydrogen's surface chemistry and its ability to prevent catalyst poisoning is determined, in part, by the nature of the carbon−catalyst interaction. For instance, if carbon−catalyst π-interactions are stronger than carbon−catalyst σ-interactions, hydrogen passivation of surface carbon will lead to large, hydrogen-terminated, sp^2/sp^3 hybridized carbon "islands" covering the catalyst surface.

Due to the preferential saturation of carbon dangling bonds with hydrogen, these islands are incapable of instigating growth and instead lead to catalyst poisoning. On the other hand, if carbon−catalyst π-interactions are weaker than carbon−catalyst σ-interactions, hydrogen passivation of surface carbon will lead to a greater proportion of sp hybridized surface carbon, which will naturally extend away from the catalyst surface (as is observed in SCC-DFTB/MD simulations, Figure S3). This keeps the nanoparticle catalytically active, but forces the nucleation process *away* from the surface, resulting in the nucleation mechanism described above. In either case, carbon aggregation on the catalyst surface remains an exothermic reaction on Al_2O_3, as it is for other catalysts. However, it is impeded kinetically by the solid phase of the catalyst, which reduces surface carbon diffusion; this point is discussed in greater detail below.

3.3. Comparison of SWCNT Nucleation on Al_2O_3, Si and Transition Metal Catalysts.

The mechanism of SWCNT nucleation on Al_2O_3 catalysts differs fundamentally from both Si-based and transition metal catalysts. Comparison of the ratios of sp-, sp^2-, and sp^3-hybridized carbon observed on Al_2O_3 with those observed on SiO_2[35] and Ni[64] nanoparticle catalysts is made in Figure 3. In each case, the method of simulation is the same (i.e., DFTB/MD), and although the growth temperature differs slightly between these three simulations (these temperatures match relevant CVD experiments for each catalyst), atomic carbon is used as the growth precursor in each case. Figure 3a shows that sp-hybridized carbons (polyyne chains) are dominant on Al_2O_3 catalysts (consistent with Figure 1), with little sp^2-hybridized and no sp^3-hybridized carbon being formed. As described above, these chains predominantly extend away from the Al_2O_3 surface. For SiO_2, sp-hybridized carbon is still dominant, but there is a much greater proportion of sp^2- and even sp^3-hybridized carbon present on the catalyst surface. The presence of sp^3-hybridized carbon, and the fact that the relative populations of sp-, sp^2-, and sp^3-hybridized carbon quickly becomes static, indicates that carbon is adsorbed strongly onto the surface structure of the nanoparticle, with very low diffusional mobility. On the other hand, Figure 3c shows that, on Ni, the populations of sp- and sp^2-hybridized carbon are dynamic, indicating a rapid sp → sp^2 conversion.

The growth of the sp-hybridized carbon chains perpendicular to the Al_2O_3 catalyst surface is consistent with the relative adsorption energies of carbon via σ- and π-bonding to the Al-terminated Al_2O_3 surface. Using DFT calculations, we obtained $E_{ads}(\sigma) = -60.96$ kcal/mol/carbon atom and $E_{ads}(\pi) = -1.38$
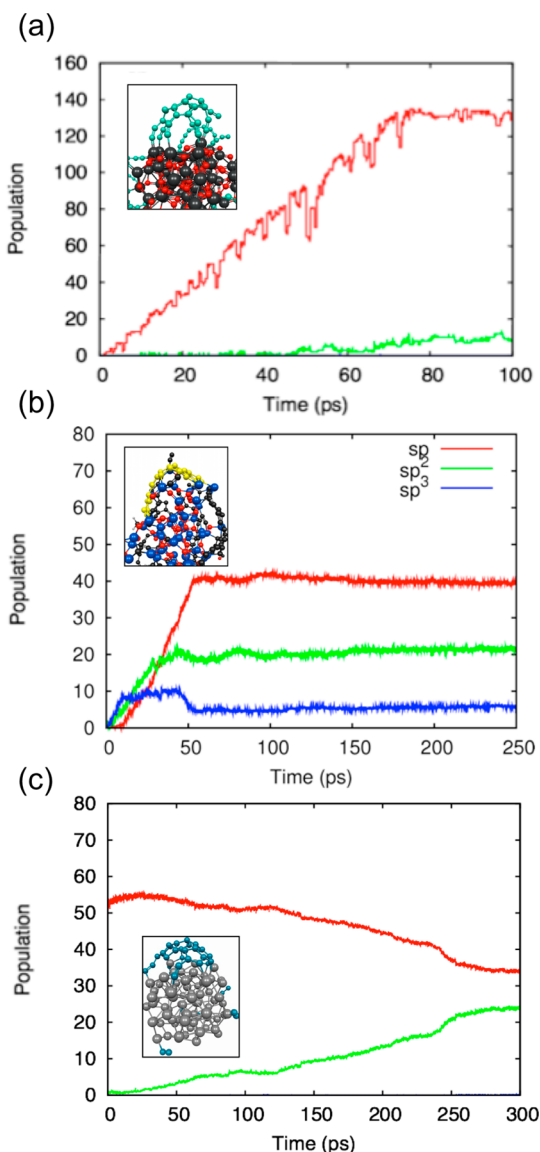

(a)

(b)

(c)

Figure 3. Evolution of sp, sp^2, and sp^3 hybridization during SWCNT nucleation on (a) Al_2O_3 (at 1100 K), (b) SiO_2 (at 1200 K)[35] (SWCNT cap indicated in yellow), and (c) Ni/Ni-carbide (at 1400 K)[64] nanoparticles (note the different scale on the vertical axis in (a)).

kcal/mol/carbon atom (see Figure 4). Including dispersion (via Grimme's[70] correction for PBE) does not significantly alter these relative adsorption strengths, with $E_{ads}(\sigma) = -70.13$ kcal/mol/carbon atom and $E_{ads}(\pi) = -1.52$ kcal/mol/carbon atom. π-bonding is therefore likely to be unfavorable at typical CVD temperatures. The formation of an extended sp^2 network adsorbed directly on the catalyst surface, as typically observed for transition metal catalysts, is therefore thermodynamically unfavorable in the case of Al_2O_3. Instead, carbon coalescence leads to predominantly sp-hybridized, carbon chains extending away from the catalyst surface. Typical growth temperatures provide enough vibrational/diffusional motion within these chains to drive sp^2 network formation via Eres' cross-linking mechanism,[38] and this process is independent of the catalyst surface. The specific example shown in Figure 1 is reminiscent of the initial stages of fullerene formation,[39] with the exception that the carbon structure is anchored to Al atoms on the Al_2O_3 surface.
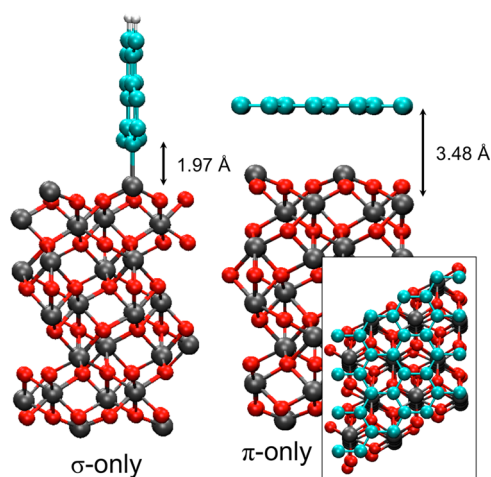
Figure 4. Comparison of σ versus π bonding between graphene and Al_2O_3 (the inset shows the "π-only" structure from above). The energy for "σ-only" adsorption is −60.96 kcal/mol/carbon atom, while the "π-only" adsorption is −1.38 kcal/mol/carbon atom.

This SWCNT nucleation mechanism is a marked departure from established nucleation mechanisms for "traditional" transition metal catalysts, and silicon-based catalysts such as Si,[34] SiC,[37] and SiO$_2$.[35,36] For these catalysts, SWCNT nucleation is surface mediated and results in more sp^2 and sp^3 carbon in the nucleating structure (Figure 3), because the nucleating SWCNT cap "sticks" more strongly to the catalyst surface. This is most notable for transition metal catalysts (illustrated in Figure 3 for Ni[64]), for which the sp/sp^2 carbon ratio is almost equal following the nucleation process. A greater portion of the catalyst surface therefore becomes covered by the nucleating carbon structure. Depending on the strength of the carbon−catalyst π-interaction, this growing carbon structure can yield SWCNT growth (weaker π interactions, such as Fe and Ni[71,72]) or catalyst poisoning (stronger π interactions, such as SiO$_2$[35]).

We note however that these phenomena cannot be explained solely on the basis of carbon−catalyst interaction strengths. For example, $E_{ads}(\pi)$ (using PBE/DZP) for graphene on Ni(111) is 0 kcal/mol.[71] Despite this similarity between $E_{ads}(\pi)$ for Al$_2$O$_3$ and Ni(111), Figure 3 shows that the nucleation mechanism differs significantly for these two catalysts. The critical difference is catalyst phase. While Al$_2$O$_3$ remains solid at these temperatures, nanoparticle Ni catalysts exist in the liquid phase.[64] Consequently, surface Ni atoms exhibit higher mobility and the catalyst is actively deformed by the nucleating carbon structure.[72−75] As a result, the carbon structure must adopt the curvature of the underlying catalyst surface, and this is achieved by the promotion of an extended sp^2 network, at the expense of sp-hybridized polyyne chains. For the same reason, diffusion of surface carbon on Al$_2$O$_3$ is anticipated to be significantly lower than diffusion on liquid/surface molten transition metal catalysts. This is consistent with SWCNT nucleation/growth on SiO$_2$,[26,28,35] which requires carbon saturation of the catalyst surface before SWCNT nucleation is observed. We therefore propose that SWCNT nucleation on Al$_2$O$_3$ occurs via a vapor−solid−solid mechanism, as it does for SiO$_2$ catalysts.

Solid oxide materials, such as SiO$_2$,[25−29] ZrO$_2$,[30] and Al$_2$O$_3$,[31] initially generated interest as SWCNT growth catalysts due to their unexpected catalytic activity, the absence of metal contaminants in the growh SWCNTs, and their potential for enabling diameter-selective and even chirality-selective CVD growth. This potential for diameter- and chirality-controlled growth is due to the catalyst remaining in the solid phase at typical CVD temperatures, making it possible to exploit epitaxy between the catalyst surface and the growing graphitic network, to preferentially produce specific (n,m) chirality SWCNTs. The most significant recent examples of this epitaxy-based approach are those of Zhou et al. (vapor-phase epitaxy on quartz),[6,8,13] Li et al. (WMo alloy nanoparticles),[12] and Fasel et al. (Pt(111)).[14] These reports demonstrate that it is possible to exploit surface epitaxy to achieve chirality control for *some* solid catalysts. However, the results of this work indicate that a solid-phase catalyst itself is not always sufficient for chirality-controlled growth. We demonstrate here a new SWCNT growth mode, one which is not directly mediated by the catalyst surface. In such a case, there is no surface epitaxy between the nucleating SWCNT cap and the catalyst surface, and so this strategy is likely to be unsuccessful. We propose that other catalysts similar to Al$_2$O$_3$ (i.e., those with weak carbon−catalyst π-interactions, strong σ-interactions, high melting points) may also fall into this class. For this class of catalysts, other experimental parameters (e.g., feedstock pressure, temperature, catalyst diameter, carbon precursor) may become more influential in achieving diameter and chirality selective growth. Investigation into this possibility is ongoing in our research groups.

4. CONCLUSION

We have presented quantum chemical simulations investigating the CVD of CH$_4$ on Al$_2$O$_3$ leading to the nucleation of SWCNTs. These simulations demonstrate for the first time an SWCNT nucleation mechanism that is not directly mediated by the catalyst surface. Instead, nucleation proceeds via the cross-linking of extended polyyne chains that are only anchored to the catalyst surface via C−Al σ-bonds. This is a significant deviation from established "vapor−liquid−solid" (VLS) and "vapor−solid−solid" (VSS) mechanisms, commonly accepted in describing nucleation on transition metal and nonmetal catalysts, respectively.[4] DFT calculations reveal that this is the product of an extremely weak π-interaction between graphitic carbon and the Al$_2$O$_3$ nanoparticle. It is expected that this weak interaction would be overcome by thermal energy at typical CVD temperatures. The role of hydrogen during SWCNT nucleation has also been established. For Al$_2$O$_3$, DFT calculations indicate that surface hydrogen can not only passivate the Al$_2$O$_3$ surface but also will preferentially form CH and CH$_2$ species, which are capable of polyyne chain formation. This prevents catalyst poisoning due to the coalescence of surface carbon species, allowing SWCNT nucleation to take place.

◼ ASSOCIATED CONTENT

ⓢ Supporting Information

Details of the model Al$_2$O$_3$ nanoparticle used in QM/MD simulations of CH$_4$ CVD; Snapshots of 10 QM/MD simulations of SWCNT nucleation. The Supporting Information is available free of charge on the ACS Publications website at DOI: 10.1021/jacs.5b02952.

◼ AUTHOR INFORMATION

Corresponding Authors
*alister.page@newcastle.edu (A.J.P.)

*sirle@chem.nagoya-u.ac.jp (S.I.)
*keiji.morokuma@emory.edu (K.M.)

Author Contributions

[⊥]A.J.P. and S.S. contributed equally.

Notes

The authors declare no competing financial interest.

■ REFERENCES

(1) Iijima, S. *Nature* **1991**, *354*, 56.
(2) Iijima, S.; Ichihashi, T. *Nature* **1993**, *363*, 603.
(3) Bethune, D. S.; Kiang, C. H.; DeVries, M. S.; Gorman, G.; Savoy, R.; Beyers, R. *Nature* **1993**, *363*, 605.
(4) Page, A. J.; Ding, F.; Irle, S.; Morokuma, K. *Rep. Prog. Phys.* **2015**, *78*, 036501.
(5) Wang, Y.; Kim, M. J.; Shan, H.; Kittrell, C.; Fan, H.; Ericson, L. M.; Hwang, W.-F.; Arepalli, S.; Hauge, R. H.; Smalley, R. E. *Nano Lett.* **2005**, *5*, 997.
(6) Liu, J.; Wang, C.; Tu, X.; Liu, B.; Chen, L.; Zheng, M.; Zhou, C. *Nat. Commun.* **2012**, *3*, 1199.
(7) Yao, Y.; Feng, C.; Zhang, J.; Liu, Z. *Nano Lett.* **2009**, *9*, 1673.
(8) Liu, B.; Liu, J.; Tu, X.; Zhang, J.; Zheng, M.; Zhou, C. *Nano Lett.* **2013**, *13*, 4416.
(9) Chiang, W.-H.; Mohan Sankaran, R. *Nat. Mater.* **2009**, *8*, 882.
(10) Li, X. L. *J. Am. Chem. Soc.* **2007**, *129*, 15770.
(11) Miyauchi, Y.; Chiashi, S.; Murakami, Y.; Hayashida, Y.; Maruyama, S. *Chem. Phys. Lett.* **2004**, *387*, 198.
(12) Yang, F.; Wang, X.; Zhang, D.; Yang, J.; Luo, D.; Xu, Z.; Wei, J.; Wang, J.-Q.; Xu, Z.; Peng, F.; Li, X.; Li, R.; Li, Y.; Li, M.; Bai, X.; Ding, F.; Li, Y. *Nature* **2014**, *510*, 522.
(13) Liu, B.; Liu, J.; Li, H.-B.; Bhola, R.; Jackson, E. A.; Scott, L. T.; Page, A.; Irle, S.; Morokuma, K.; Zhou, C. *Nano Lett.* **2015**, *15*, 586.
(14) Sanchez-Valencia, J. R.; Dienel, T.; Groning, O.; Shorubalko, I.; Mueller, A.; Jansen, M.; Amsharov, K.; Ruffieux, P.; Fasel, R. *Nature* **2014**, *512*, 61.
(15) Fort, E. H.; Donovan, P. M.; Scott, L. T. *J. Am. Chem. Soc.* **2009**, *131*, 16006.
(16) Fort, E. H.; Scott, L. T. *Angew. Chem., Int. Ed.* **2010**, *49*, 6626.
(17) Cheng, D.; Barcaro, G.; Charlier, J. C.; Hou, M.; Fortunelli, A. *J. Phys. Chem. C* **2011**, *115*, 10537.
(18) Fort, E. H.; Scott, L. T. *J. Mater. Chem.* **2011**, *21*, 1373.
(19) Fort, E. H.; Scott, L. T. *Tetrahedron Lett.* **2011**, *52*, 2051.
(20) Jasti, R.; Bertozzi, C. R. *Chem. Phys. Lett.* **2010**, *494*, 1.
(21) Omachi, H.; Nakayama, T.; Takahashi, E.; Segawa, Y.; Itami, K. *Nat. Chem.* **2013**, *5*, 572.
(22) Takagi, D.; Hibino, H.; Suzuki, S.; Kobayashi, Y.; Homma, Y. *Nano Lett.* **2007**, *7*, 2272.
(23) Kusunoki, M.; Rokkaku, M.; Suzuki, T. *Appl. Phys. Lett.* **1997**, *71*, 2620.
(24) Wang, Z.; Irle, S.; Zheng, G.; Kusunoki, M.; Morokuma, K. *J. Phys. Chem. C* **2007**, *111*, 12960.
(25) Bachmatiuk, A.; Boàrrnert, F.; Grobosch, M.; Schàffel, F.; Wolff, U.; Scott, A.; Zaka, M.; Warner, J. H.; Klingeler, R.; Knupfer, M.; Buàchner, B.; Ruàmmeli, M. H. *ACS Nano* **2009**, *3*, 4098.
(26) Huang, S.; Cai, Q.; Chen, J.; Qian, Y.; Zhang, L. *J. Am. Chem. Soc.* **2009**, *131*, 2094.
(27) Liu, B.; Ren, W.; Liu, C.; Sun, C.-H.; Gao, L.; Li, S.; Jiang, C.; Cheng, H.-M. *ACS Nano* **2009**, *3*, 3421.
(28) Liu, H.; Takagi, D.; Chiashi, S.; Homma, Y. *Carbon* **2010**, *48*, 114.
(29) Wang, H.; Wei, L.; Ren, F.; Wang, Q.; Pfefferle, L. D.; Haller, G. L.; Chen, Y. *ACS Nano* **2013**, *7*, 614.
(30) Steiner, S. A.; Baumann, T. F.; Bayer, B. C.; Blume, R.; Worsley, M. A.; MoberlyChan, W. J.; Shaw, E. L.; Schlögl, R.; Hart, A. J.; Hofmann, S.; Wardle, B. L. *J. Am. Chem. Soc.* **2009**, *131*, 12144.
(31) Liu, H.; Takagi, D.; Ohno, H.; Chiashi, S.; Chokan, T.; Homma, Y. *Appl. Phys. Express* **2008**, *1*, 014001.
(32) Takagi, D.; Kobayashi, Y.; Homma, Y. *J. Am. Chem. Soc.* **2009**, *131*, 6922.
(33) Rao, F.; Li, T.; Wang, Y. *Carbon* **2009**, *47*, 3580.
(34) Chandrakumar, K. R. S.; Page, A. J.; Irle, S.; Morokuma, K. *J. Phys. Chem. C* **2013**, *117*, 4238.
(35) Page, A. J.; Chandrakumar, K. R. S.; Irle, S.; Morokuma, K. *J. Am. Chem. Soc.* **2011**, *133*, 621.
(36) Page, A. J.; Chandrakumar, K. R. S.; Irle, S.; Morokuma, K. *Chem. Phys. Lett.* **2011**, *508*, 235.
(37) Page, A. J.; Chandrakumar, K. R. S.; Irle, S.; Morokuma, K. *Phys. Chem. Chem. Phys.* **2011**, *13*, 15673.
(38) Eres, G.; Rouleau, C. M.; Yoon, M.; Puretzky, A. A.; Jackson, J. J.; Geohegan, D. B. *J. Phys. Chem. C* **2009**, *113*, 15484.
(39) Irle, S.; Zheng, G.; Wang, Z.; Morokuma, K. *J. Phys. Chem. B* **2006**, *110*, 14531.
(40) Elstner, M.; Porezag, D.; Jungnickel, G.; Elsner, J.; Haugk, M.; Frauenheim, T.; Suhai, S.; Seifert, G. *Phys. Rev. B: Condens. Matter Mater. Phys.* **1998**, *58*, 7260.
(41) Aradi, B.; Hourahine, B.; Frauenheim, T. *J. Phys. Chem. A* **2007**, *111*, 5678.
(42) Luschtinetz, R.; Oliveira, A. F.; Frenzel, J.; Joswig, J.-O.; Seifert, G.; Duarte, H. A. *Surf. Sci.* **2008**, *602*, 1347.
(43) Swope, W. C.; Andersen, H. C.; Berens, P. H.; Wilson, K. R. *J. Chem. Phys.* **1982**, *76*, 637.
(44) Martyna, G. J.; Klein, M. L.; Tuckerman, M. *J. Chem. Phys.* **1992**, *97*, 2635.
(45) Nose, S. *J. Chem. Phys.* **1984**, *81*, 511.
(46) Wagner, F.; Laloyaux, T.; Scheffler, M. *Phys. Rev. B: Condens. Matter Mater. Phys.* **1998**, *57*, 2102.
(47) Weinert, M.; Davenport, J. W. *Phys. Rev. B: Condens. Matter Mater. Phys.* **1992**, *45*, 13709.
(48) Wentzcovitch, R. M.; Martins, J. L.; Allen, P. B. *Phys. Rev. B: Condens. Matter Mater. Phys.* **1992**, *45*, 11372.
(49) Page, A. J.; Irle, S.; Morokuma, K. *J. Phys. Chem. C* **2010**, *114*, 8206.
(50) Page, A. J.; Minami, S.; Ohta, Y.; Irle, S.; Morokuma, K. *Carbon* **2010**, *48*, 3014.
(51) Page, A. J.; Ohta, Y.; Irle, S.; Morokuma, K. *Acc. Chem. Res.* **2010**, *43*, 1375.
(52) Wang, Y.; Page, A. J.; Nishimoto, Y.; Qian, H.-J.; Morokuma, K.; Irle, S. *J. Am. Chem. Soc.* **2011**, *133*, 18837.
(53) Kim, J.; Page, A. J.; Irle, S.; Morokuma, K. *J. Am. Chem. Soc.* **2012**, *134*, 9311.
(54) Perdew, J. P.; Chevary, J. A.; Vosko, S. H.; Jackson, K. A.; Pederson, M. R.; Singh, D. J.; Fiolhais, C. *Phys. Rev. B: Condens. Matter Mater. Phys.* **1992**, *46*, 6671.
(55) Soler, J. M.; Artacho, E.; Gale, J. D.; Garcia, A.; Junquera, J.; Ordejón, P.; Sánchez-Portal, D. *J. Phys.: Condens. Matter* **2002**, *14*, 2745.
(56) Page, A. J.; Ohta, Y.; Okamoto, Y.; Irle, S.; Morokuma, K. *J. Phys. Chem. C* **2009**, *113*, 20198.

(57) Kirfel, A.; Eichhorn, K. *Acta Crystallogr., Sect. A: Found. Crystallogr.* **1990**, *46*, 271.

(58) Saha, B.; Shindo, S.; Irle, S.; Morokuma, K. *ACS Nano* **2009**, *3*, 2241.

(59) Li, H.-B.; Page, A. J.; Irle, S.; Morokuma, K. *J. Phys. Chem. Lett.* **2013**, *4*, 2323.

(60) Hu, J. G.; Zhang, Y. S.; Jia, L. C.; Zhu, B.; Yang, H. G.; Zhan, Q. *Adv. Mater. Res.* **2011**, *399–401*, 2261.

(61) Note that, although the carbon addition rate is the same in all trajectories, the rate at which carbon adsorbs to the nanoparticle surface will be different. This is because of the unpredictable nature of the nanoparticle CH_x collisions.

(62) Silvearv, F.; Larsson, P.; Jones, S. L. T.; Ahuja, R.; Larsson, J. A. *J. Mater. Chem. C* **2015**, *3*, 3422.

(63) Ohta, Y.; Okamoto, Y.; Page, A. J.; Irle, S.; Morokuma, K. *ACS Nano* **2009**, *3*, 3413.

(64) Page, A. J.; Yamane, H.; Ohta, Y.; Irle, S.; Morokuma, K. *J. Am. Chem. Soc.* **2010**, *132*, 15699.

(65) Thess, A.; Lee, R.; Nikolaev, P.; Dai, H.; Petit, P.; Robert, J.; Xu, C.; Lee, Y. H.; Kim, S. G.; Rinzler, A. G.; Colbert, D. T.; Scuseria, G. E.; Tomanek, D.; Fischer, J. E.; Smalley, R. E. *Science* **1996**, *273*, 483.

(66) Mora, E.; Pigos, J. M.; Ding, F.; Yakobson, B. I.; Harutyunyan, A. R. *J. Am. Chem. Soc.* **2008**, *130*, 11840.

(67) Wang, Y.; Gao, X.; Qian, H.-J.; Ohta, Y.; Wu, X.; Eres, G.; Morokuma, K.; Irle, S. *Carbon* **2014**, *72*, 22.

(68) Oguri, T.; Shimamura, K.; Shibuta, Y.; Shimojo, F.; Yamaguchi, S. *Chem. Phys. Lett.* **2014**, *595–596*, 185.

(69) Shibuta, Y.; Arifin, R.; Shimamura, K.; Oguri, T.; Shimojo, F.; Yamaguchi, S. *Chem. Phys. Lett.* **2013**, *565*, 92.

(70) Grimme, S. *J. Comput. Chem.* **2006**, *27*, 1787.

(71) Page, A. J.; Wang, Y.; Li, H.-B.; Irle, S.; Morokuma, K. *J. Phys. Chem. C* **2013**, *117*, 14858.

(72) Li, H.-B.; Page, A. J.; Hettich, C.; Aradi, B.; Köhler, C.; Frauenheim, T.; Irle, S.; Morokuma, K. *Chem. Sci.* **2014**, *5*, 3493.

(73) Wang, Y.; Page, A. J.; Li, H.-B.; Qian, H.-J.; Jiao, M.-g.; Wu, Z.-J.; Morokuma, K.; Irle, S. *Nanoscale* **2014**, *6*, 140.

(74) Gomez-Gualdron, D. A.; McKenzie, G. D.; Alvarado, J. F. J.; Balbuena, P. B. *ACS Nano* **2012**, *6*, 720.

(75) Li, H.-B.; Page, A. J.; Wang, Y.; Irle, S.; Morokuma, K. *Chem. Commun.* **2012**, *48*, 7937.